Computers & Fluids xxx (2011) xxx–xxx

Contents lists available at ScienceDirect

Computers & Fluids

journal homepage: www.elsevier.com/locate/compfluid

Starting jet flows in a three-dimensional channel with larynx-shaped constriction

Rüdiger Schwarze *, Willy Mattheus, Jens Klostermann, Christoph Brücker

Institut für Mechanik und Fluiddynamik, TU Bergakademie Freiberg, Lampadiusstr. 4, 09596 Freiberg, Germany

ARTICLE INFO

Article history:
Received 2 June 2009
Received in revised form 21 March 2011
Accepted 31 March 2011
Available online xxxx

Keywords:
Glottal airflow
Elliptic jet
Instability
Jet breakdown
Numerical simulation
Larynx-shaped channel
Starting jet flow
Numerical model
Validation

ABSTRACT

A numerical model for the three-dimensional starting jet flow in a channel with a static larynx-shaped constriction is presented. Detailed resolution of this kind of jet flow is necessary in order to understand the complex coupling between flow and acoustics in the process of human phonation. The numerical model is based on the equation of continuity and the Navier–Stokes equations. The investigations are done with the open source CFD package OpenFOAM. Numerical simulations are performed for a square-sectioned channel geometry, which is constricted with a fixed shape conforming to the fully opened human glottis. Time-dependent inflow boundary conditions are applied in order to model transient glottal flow rates. The setup of the numerical simulations corresponds to the configuration of a model experiment in order to allow detailed validation. The numerical results are in good agreement with the experimental data, when the near-wall region in the glottal gap is adequately resolved by the numerical grid. The results illustrate the complex interactions between the jet flow and the surrounding vortices.

1. Introduction

Human voice is produced by the pulsating airflow generated during the self-sustained oscillations of the vocal folds. Actually, the physics of this phenomenon with emphasize on the interactions between the vocal folds oscillation, the aerodynamics of the airflow and the acoustics of the generated sound is a highly active field of interdisciplinary research, see e.g. [1]. Fluid mechanics research is done with experimental models or with numerical simulations. Among others, some important effects which have been studied in the past by means of computational fluid dynamics (CFD) are flow separation in the glottis [2,3], Coanda effect [4,5], intraglottal pressure distribution [3,4,6], glottal airflow rate [1,3,7], pulsating air jet flows [8–10] and supraglottal jet turbulence [5].

The nonacoustic fluid motion of the air in the glottis provides a source of sound, with the monopole source associated to the pulsating air flow and dipole as well as quadrupole source terms which arise from the mutual interactions of vortical structures and the supraglottal jet with the walls. It is generally accepted that flow separation in the glottis has a major effect on the pressure field and the jet flow in the supraglottal region, see e.g. [2]. There are several papers which investigate flow separation in the glottis by means of numerical simulations with lower-dimensional numerical models, e.g. [1,3]. These models have special treatments for the correct prediction of flow separation. On the contrary the transient three-dimensional supraglottal flow field consisting of the jet and the induced vortex structures has been studied only experimentally so far [11–13]. Previous numerical studies of the three-dimensional supraglottal flow have been focused on the laryngeal jet during aspiration, e.g. [14,15].

In the paper, we investigate the starting glottal jet downstream of a rigid glottis-shaped constriction. The flow is similar but not identical to the well-known starting round jet flow, which kinematics and dynamics has been investigated in detail in the past years [16–21]. Gharib and coworkers [16–18,20] introduced the formation number of a vortex ring which is generated through an impulsively starting jet. The formation number characterizes the separation of the vorticity field of the leading vortex from the trailing jet [16]. The formation number of a starting jet flow can be varied by the modification of jet acceleration scenario or the orifice shape [19]. By the inspection of the vortex dynamics, Krueger and Gharib [20] found that impulse transfer from the starting round jet to the surrounding fluid is maximized at the formation number. Due to the symmetry of the problem, it is also possible to describe the pinch-off process of the leading vortex from the jet by analytical models [18,21].

Our paper presents a fully three-dimensional numerical model of the starting glottal jet flow in order to study the transient flow downstream of the glottis-shaped constriction in detail. Numerical simulations are carried out for a square-sectioned channel with a glottis-shaped constriction.

* Corresponding author. Tel.: +49 3731 392486; fax: +49 3731 393455.
E-mail address: Ruediger.Schwarze@imfd.tu-freiberg.de (R. Schwarze).

0045-7930/$ - see front matter © 2011 Published by Elsevier Ltd.
doi:10.1016/j.compfluid.2011.03.016

The geometry of the numerical model follows the setup of the experimental model of Triep et al [11]. The numerical model is implemented in the open CFD library OpenFOAM. A detailed description of the numerical model is given. The numerical simulations are done in the absence of fluid-structure interactions. A comparison of the numerical results with corresponding flow data is given.

The scope of the paper is to resolve details of the kinematics and dynamics of the starting glottal jet. Therefore the basic mechanisms of the transient development, i.e. flow separation, formation of the leading vortex and interactions between the leading vortex and the trailing jet are investigated.

The paper presents a status report of an ongoing research project. Systematic investigations of oscillating airflows in a glottis-shaped channel will be given in a separate paper.

2. Numerical model

2.1. Glottal channel

The geometry parameters of the numerical model corresponds to a water model experiment of the flow in a square-sectioned channel with a glottis-shaped constriction in order to allow validation by comparison with corresponding flow data. Photographs which show the setup of the water model are given in Fig. 1.

The experimental setup is in principle a U-shaped channel composed of a test section with a vertical liquid column at each end, see Fig. 1a. All channel components are made of Perspex in order to have full optical accessibility into the transparent liquid medium. Included into the test section is the non-transparent glottis-shaped constriction, Fig. 1b. The glottis geometry is replicated by two cams, which model the upper and the lower vocal fold. Each of the cams is pivoted in a wedge, then covered with a silicone membrane and arranged vis-a-vis in the test section of the channel. The geometric data for the glottis is given in Table 1.

Note that this cam model is a 3:1 scale-up of a typical human glottis. Flow is induced by imposing a pressure head across the model glottis through a difference in the up- and downstream liquid column heights. According to the fluid dynamical similarity laws and considering water as the working medium, the pressure head in the model is of half the value compared to the value in natural phonation and velocities are of the order of 1 m/s. This fluid dynamical time scale allows a better way to visualize the glottal jet in the experiment and to extract velocity data of the flow field by means of Particle-Image Velocimetry. More details of the water model experiment are given by Triep et al. [11].

Fig. 2 gives the geometry of computational domain, which is used in the numerical simulations. The computational domain encompasses the test section of the water model. It is expected, that the homogeneous flow upstream of the glottis has little influence on the structure of the supraglottal flow. Hence, the subglottal flow region is reduced to a short inflow neck on the left-hand side of the glottal constriction. The global dimensions of the computational domain are $L \times H \times W = 200\ \text{mm} \times 60\ \text{mm} \times 60\ \text{mm}$ (due to the 3:1 upscaling). The boundaries of the computational domain correspond to the inner contour of the test section (upper, lower, front and back walls) with additional inlet (left) and outlet (right) boundary.

Table 1
Characteristic parameters of the glottal constriction in the numerical model according to Triep et al. [11].

Parameter	Value
α	45°
β	80°
w^{max}	8 mm
H	60 mm
W	60 mm

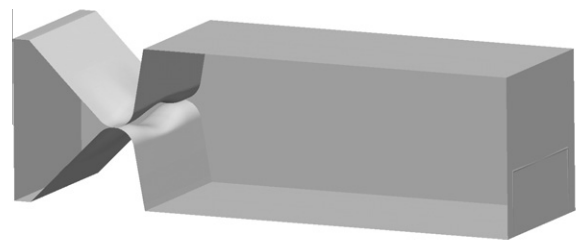

Fig. 2. Geometry of the computational domain.

Details of the computational domain with the channel and the glottal constriction are sketched in Fig. 3. The characteristic parameters of the constriction are the angles α and β, the maximum opening width w^{max} of the glottis and finally the height H and width W of the supraglottal channel. The dimensions of these parameters which are implemented in the computational grids are given in Table 1. With H and W, the hydraulic equivalent diameter D of the channel becomes 60 mm.

The characteristic parameters of the glottal constriction correspond identically to the parameters of the water model experiment of Triep et al. [11]. A discussion of the similarity of the flow in the experiment and the numerical simulations with the real flow in the human glottis is also given by Triep et al. [11]. In summary, the flows in the numerical simulations meet Reynolds and Strouhal similarity to the real laryngeal flows. Since the Mach number is less than 0.1, the flow can be treated as incompressible. Therefore significant structures of the laryngeal flow can be resolved by incompressible flows in a water model experiment or a corresponding numerical simulation, respectively.

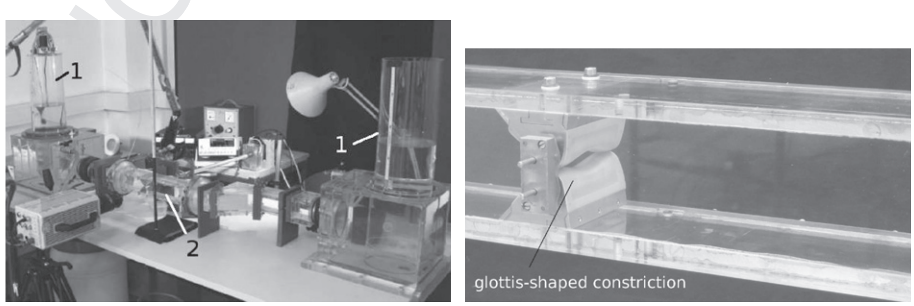

(a) U-shaped channel with liquid columns (1) and test section (2).

(b) Zoom into the test section with cam model of the glottis.

Fig. 1. Water model of the glottal channel with glottis-shaped constriction.

Please cite this article in press as: Schwarze R et al. Starting jet flows in a three-dimensional channel with larynx-shaped constriction. Comput Fluids (2011), doi:10.1016/j.compfluid.2011.03.016

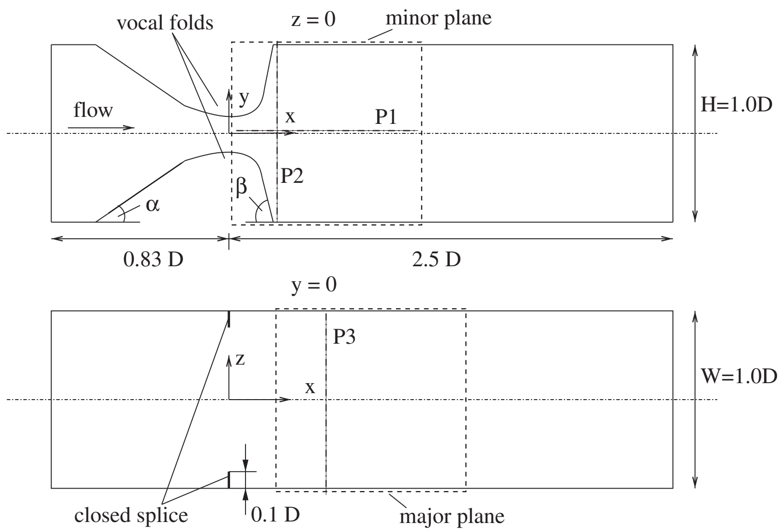

Fig. 3. Geometry of the computational model for the glottal channel, major and minor plane, baselines P1, P2 and P3 are employed for inspection of flow data.

2.2. Measurements of the starting flow

In the experiments, the starting jet flow is generated by a jump-like opening of a valve in the pressure chamber connected to the subglottal channel. The pressure head is realized by a difference of the sub- and supraglottal water level heights, which is hold by a magnetic valve above the subglottal water level. The flow is started by the opening of the magnetic valve. Then, the flow rate Q starts from zero and reaches the maximum value after a period $\tau = 700$ ms because the sub- and supraglottal water level heights are balanced by the flow.

In the water model experiment, the time-dependent behavior of Q is recorded. PIV measurements have been carried out in the major and minor planes indicated in Fig. 3. The major plane reaches from $(x,z) = (0.2\ D, -0.5\ D)$ (lower left corner) to $(x,z) = (1.2\ D, 0.5\ D)$ (upper right corner). The minor plane reaches from $(x,y) = (0, -0.5\ D)$ (lower left corner) to $(x,y) = (1.0\ D, 0.5\ D)$ (upper right corner).

The measurements have been repeated in order to obtain an ensemble of 10 realizations of the starting flow. From these measurements, ensemble averaged flow data are available. Later, vorticity fields from the experiment and the simulations are compared in the major and minor plane. Additionally, velocity profiles are compared along baselines P1 (x-axis), P2 ($x = 0.2\ D, z = 0$) and P3 ($x = 0.5\ D, y = 0$).

2.3. Governing equations and model assumptions

The incompressible flow in the glottal channel will exhibit a transitional behavior. Starting with completely laminar flow conditions, the flow becomes super-critical in the glottal region after some acceleration. Then transition to turbulence is observed downstream of the glottal constriction. The CFD model which should describe both the laminar and the turbulent flow regime is based on the Navier–Stokes equations for incompressible, viscid flows

$$\frac{\partial u_j}{\partial x_j} = 0 \qquad (1)$$

$$\frac{\partial u_i}{\partial t} + u_j \frac{\partial u_i}{\partial x_j} = -\frac{1}{\rho}\frac{\partial p}{\partial x_i} + \nu \frac{\partial u_i^2}{\partial x_j^2} \qquad (2)$$

in combination with high-order numerical discretisation schemes. In Eqs. (1) and (2) u is the flow velocity and p is the pressure. The material parameters of water are density $\rho = 10^3$ kg/m^3 and kinematic viscosity $\nu = 10^{-6}$ m^2/s. The numerical schemes are described in detail in the next sections.

The numerical setup is assumed to provide a blending between a direct computation of the laminar flow regions and an implicit Large-Eddy Simulation (ILES) [22,23] for the transitional and the turbulent flow regions. ILES has been successfully applied in numerical simulations of transitional square jet flows [24] and decaying vortex flows [25]. In these studies, the behavior of large coherent structures around non-circular jets and energy transfer from the large coherent to the turbulent structures have been resolved in good agreement with experimental observations and direct numerical simulations, respectively. These effects dominate the flow downstream of the glottal constriction, too. Therefore the ILES approach is assumed to work well in the present problem.

2.4. Numerical scenario and boundary conditions

As discussed above, the focus of the numerical investigations is the correct description of the developing supraglottal flow structures, namely the starting supraglottal jet, the vortex structures and their interactions. Because fluid-structure interactions in the glottis are neglected in this first approach, the glottal opening is kept fixed throughout the simulations. Therefore, the numerical scenario is based on a time-dependent behavior of the flow rate $Q(t)$ in the channel, which has been measured in the water model experiment.

A velocity inlet condition $\underline{u}^{in} = (u^{in}(t), 0, 0)$ for the numerical simulations is derived from $Q(t)$. The velocity inlet drives the global flow in the laryngeal channel. The time-dependent velocity function $u^{in}(t)$ is shown in Fig. 4. The Reynolds number Re based on the hydraulic equivalent diameter $d = 8.7$ mm of the glottis gap is also given in the figure, with a maximum value around $Re \approx 8800$. A pressure outlet with a gauge pressure $p^{out} = 0$ Pa with respect to the static pressure head of the downstream liquid column is applied at the outflow of the channel. Finally, the no-slip condition $\underline{u}^{wall} = 0$ m/s is applied at the rigid walls of the domain.

From the experiments, it is found that the turbulence intensity in the subglottal domain upstream of the glottal constriction is far below 1%. Therefore an explicit velocity fluctuation is not prescribed at the inlet boundary. The transition of the flow occurs downstream of the glottis.

Please cite this article in press as: Schwarze R et al. Starting jet flows in a three-dimensional channel with larynx-shaped constriction. Comput Fluids (2011), doi:10.1016/j.compfluid.2011.03.016

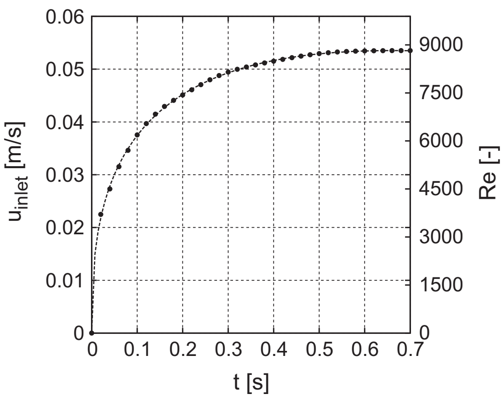

Fig. 4. Inlet velocity function $u^{in}(t)$ applied in the simulations, dots indicate measured values from the experiment.

2.5. Computational grid

A block-structured approach is employed in order to mesh the computational domain in Fig. 2. Here, attention has been paid to a regular resolution of the overall flow domain, which is discretized into grids with three different grid resolutions, Fig. 5. The first grid (fine mesh with wall resolution – **FMWR**) consists of about 5,000,000 grid cells and special attention has been paid for a fine resolution of the near-wall cells in the glottal gap, Fig. 5a.

Here, the dimensionless wall distance of the wall-nearest node is $y^+ = O(1)$ almost everywhere in the glottal opening. In order to achieve $y^+ = O(1)$, the values of y^+ in the wall-adjacent cells in the glottis have been checked after test calculations. If necessary, the near-wall grid has been re-arranged until $y^+ = O(1)$ is fulfilled throughout the complete simulation period.

The second grid (fine mesh without wall resolution – **FM**) consists of 3.000.000 grid cells. In the glottis, it has approximately the same grid resolution in the core flow region as grid FMWR, but there is no near-wall grid refinement in the glottal gap, Fig. 5b. The third grid (coarse mesh with wall resolution – **WR**) consists of only 1,000,000 grid cells, with a similar near-wall grid resolution than in grid FMWR but a less dense spacing in the core flow region, Fig. 5c.

With the near-wall grid refinement in grids FMWR and WR, we assume that two important structures of the flow are sufficiently resolved:

1. the flow separation line at the diverging part of the glottal constriction,
2. the velocity distribution in the separating laminar boundary layers, which determine the velocity distribution in the free shear layers of the jet.

Special attention has been paid to the meshing of the glottal constriction. Here geometric singularities result from the touching of the two curved faces of the lower and the upper vocal fold, see Fig. 6b. Meshing of this part is crucial but high mesh quality has to be maintained due to the developing shear layers in this region. Therefore the geometry is slightly modified at the region of touching faces. A tiny closed splice of 0.1 mm height and 6 mm length is introduced in the outer part of the glottal gap, Fig. 6b. The location of the closed splice is indicated in Fig. 3. With the closed splice, block-structured meshing is possible in this region.

2.6. Numerics

Eqs. (1) and (2) are integrated with the CFD library OpenFOAM [26]. OpenFOAM uses the finite-volume method in cell-centered formulation in order to solve systems of partial differential equations on 3D block-structured or unstructured meshes. OpenFOAM has been already successfully employed in the context of both laminar and ILES flow computations [25,28].

A TVD scheme with a flux limiter function $\psi(r) = max[0, min(2 \cdot r, 1)]$ [27] is employed for interpolation of the convective flux terms in the simulations. The smoothness parameter r is defined by the ratio of consecutive gradients. The choice of the TVD scheme is in line with the findings of Grinstein et al. [29], who note that TVD schemes with local constraints should be preferred in the context of ILES.

The 2nd order central differencing scheme (CDS) is used for the discretization of the diffusive fluxes. Two different schemes are employed for time integration of Eqs. (1) and (2): a first order scheme (annotation **CNE** in the figures in Section 3) which blends the Crank-Nicolson scheme with a weighting factor of 0.8 and the Euler implicit scheme with a weighting factor of 0.2 and the second-order three-level backward differencing scheme (annotation **BW**). Four

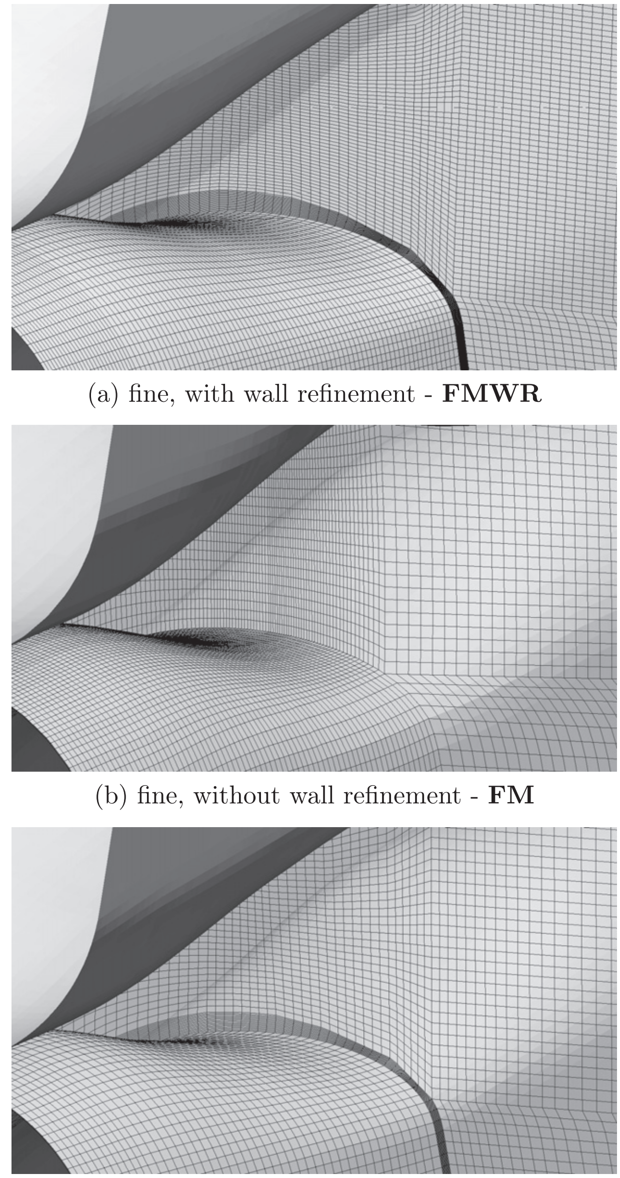

(a) fine, with wall refinement - **FMWR**

(b) fine, without wall refinement - **FM**

(c) coarse, with wall refinement - **WR**

Fig. 5. Computational grids: near-wall treatment in the glottis.

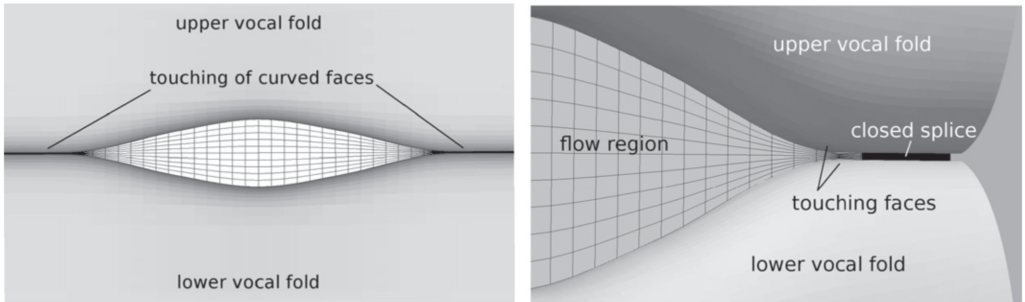

(a) cross section through the glottal gap (b) closed splice in the glottal gap (figure is stretched in vertical direction)

Fig. 6. Computational grid near the vocal folds (coarsed illustration of the grid in the flow region).

different time-step sizes $\Delta t_1 = 20\,\mu s, \Delta t_2 = 10\,\mu s, \Delta t_3 = 5\,\mu s$ and $\Delta t_4 = 2.5\,\mu s$ are employed in the simulations.

The blending has been introduced because the combination of the TVD, CDS and pure Crank-Nicolson schemes was found to be only marginally stable in the simulations. During the transition to turbulence, increasing high-frequency nonlinearities have led to diverging solution behavior. Typically artificial dissipation should be increased in the convective terms in order to circumvent these problems. However this would influence the effect of the TVD scheme and therefore the performance of the ILES approach. Therefore we employ the blended time integration scheme in order to stabilize the solution behavior. Due to the small time-step, the 1st order CNE scheme should be acceptable, which will be proven by comparison with results from the BW simulations.

Mass conservation is enforced with the transient PISO algorithm [30] with a collocated arrangement of pressure and velocity. The formulation of the algorithm is in line with the Rhie and Chow correction [31] in order to avoid non-physical oscillations in the flow variables.

The pressure equation is solved with an algebraic multi-grid solver with line Gauss-Seidel smoothing. The solver operates in the sawtooth cycle with a summation operator for restriction and an injection operator for prolongation. The momentum equations are solved with the biconjugate gradient algorithm of Fletcher [32], where incomplete LU decomposition is used for preconditioning the system.

The residual errors per time-step are of the order 10^{-7} for the momentum equation and of the order of 10^{-8} for the pressure equation.

The simulations have been carried out on the high performance computers SGI Altix 4700 (featured with 1024 dual-core Intel Itanium processors) and PC farm Deimos (724 heterogeneous compute nodes featured with 1, 2 or 4 AMD Opteron Dual Core CPUs) at the Center for Information Services and High Performance Computing (ZIH) of the TU Dresden. For parallel computing, the grids have been divided into 64, 96 or 128 partitions due to the METIS method [33,34], respectively.

3. Results

3.1. Transient flow structure

The development of the elliptic jet in the supraglottal channel can be visualized by regions of concentrated vorticity $\underline{\Omega} = \nabla \times \underline{u}$. Fig. 7 gives characteristic snapshots from the emsemble-averaged PIV measurements and the CFD simulations. The subfigures show the major plane where important structures of the flow field are indicated by the amplitude $\|\Omega_y\|$ of the y component of $\underline{\Omega}$. The locations of the major and the minor plane are indicated in Fig. 3, respectively. The scale of $\|\Omega_y\|$ is given in sub Fig. 7c. The jet flow direction is indicated by the arrow (a).

It can be seen that the leading vortex ring, which is intersected by the major plane in (b), penetrates the quiescent fluid in the supraglottal region. The stretched regions of large vorticity amplitudes (c) are expected to represent the shear layers of the developing supraglottal jet flow, whereas compact regions of large vorticity should correspond to cross sections through vortex tubes.

Figs. 8 and 9 show the development of the supraglottal jet flow which is observed in the PIV measurements and in the numerical simulations on grid FMWR. Fig. 8 displays the major plane with the amplitude of the y component, Fig. 9 displays the minor plane with the amplitude of the z component of $\underline{\Omega}$.

As a dominating effect, axis switching is observed in the experiment as well as in the numerical simulation: In the developing jet, the jet width w_z in the major plane decreases strongly downstream of the constriction, Fig. 8a and c, whereas the jet width w_y in the minor plane is slightly increased, Fig. 9a and b. These observations are in agreement with the findings of Hussain and Husain [35,36] for developing elliptic jets.

In the ensemble-averaged data from the PIV measurements, the flow structures are obviously blurred. We assume that the jet shear layers in the experiment are excited by some small-scale disturbances in the glottal region due to small background noise in the experiments. Additionally small displacements between the individual realizations of the ensemble may be responsible for the blurring of the PIV data.

However, besides the small differences the overall development of the starting elliptic jet agrees well in experiment and numerical simulation.

The effects of the near-wall grid refinement is visualized in Figs. 10 and 11, where the jet development in the minor (Fig. 10) and the major plane (Fig. 11) are compared for the three grids (i) FMWR, (ii) FM and (iii) WR. It is evident, that the jet shape, the axis switching (with the increase and the decrease of the jet minor and major axis) and the transition to turbulence are similar resolved on the two grids FMWR and WR with wall refinement.

On the contrary, these phenomena are resolved in different mode on grid FM without wall refinement. Especially, the increase and the decrease of the jet minor and major axis are strongly overestimated in comparison with the experimental findings in Figs. 8 and 9. Consequently, the stronger deceleration of the mean flow of the elliptic jet induces a higher turbulence intensity downstream of the trailing edge of the jet.

The influence of the time discretization on the flow resolution is visualized in Fig. 12. Here, simulation results which are obtained with different time integration schemes (CNE and BW) as well as different time-step sizes (Δt_2 and Δt_3) are compared. Obviously

Please cite this article in press as: Schwarze R et al. Starting jet flows in a three-dimensional channel with larynx-shaped constriction. Comput Fluids (2011), doi:10.1016/j.compfluid.2011.03.016

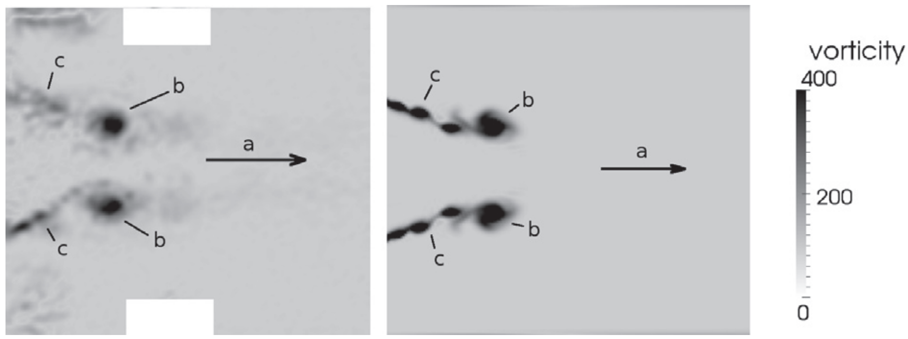

(a) PIV (b) CFD (c) scale of $\|\Omega_y\|$ in s^{-1}

Fig. 7. Jet development in the major plane, main characteristics indicated by $\|\Omega_y\|$: (a) flow direction, (b) leading vortex, (c) jet shear layers.

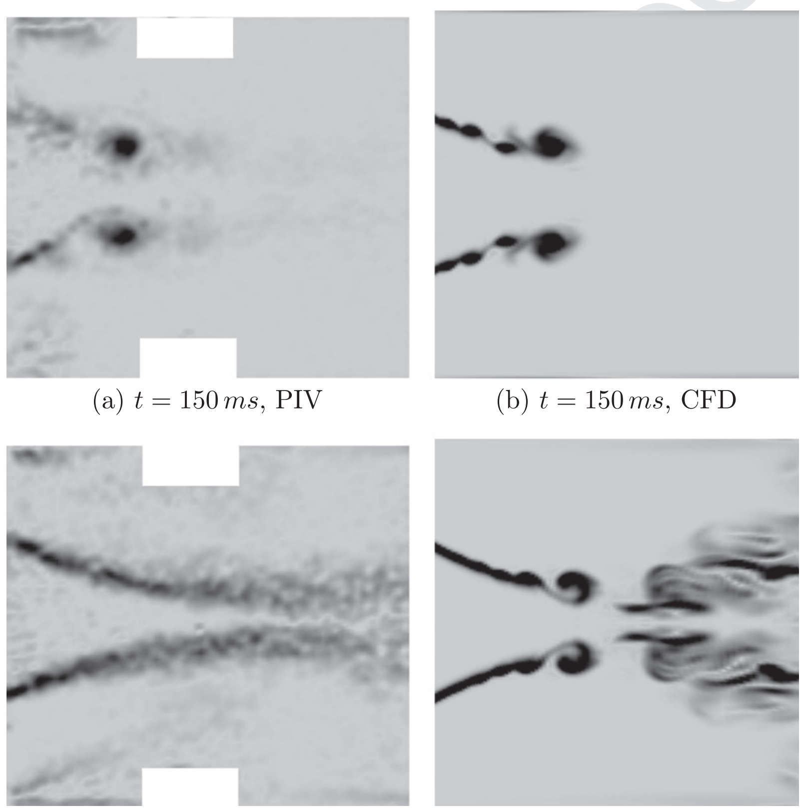

(a) $t = 150\,ms$, PIV (b) $t = 150\,ms$, CFD

(c) $t = 600\,ms$, PIV (d) $t = 600\,ms$, CFD

Fig. 8. Jet development in the major plane, indicated by $\|\Omega_y\|$ with the scale in Fig. 7c.

the influence of the time discretization on a specific grid is much smaller than the previously discussed impact of the grid on the quality of flow resolution.

3.2. Velocity profiles

For a more quantitative comparison between the different numerical results and the experimental measurements, profiles of the velocity in x-direction $u(x/H)$ along the baselines P1, P2 and P3, see Fig. 3, are inspected.

Fig. 13 shows an exemple of the velocity profile from the numerical simulation with grid FMWR at flow time $t = 450$ ms. In the velocity profile, two different regions can be identified. Region (i) gives the nearly constant velocity in the developed core of the elliptic jet. Region (ii) is dominated by the large coherent vortex structures, which have been developed from the jet shear layers. The coherent structures reach the jet centerline around $x/H = 0.6$ where the two shear layers come close to each other. Downstream of this point, they induce an acceleration and deceleration of the jet axial velocity similar to a wave train.

Fig. 14 compares the numerical (FMWR, FM, WR) and experimental (PIV) velocity profiles at baseline P1 for four different flow times t. The experimental velocity profile gives the ensemble-averaged PIV data. Here error bars indicate the uncertainty in the reported measurements.

In all subfigures, the numerical simulations on grids FMWR and WR fit reasonably to the experimental measurements for $x \leqslant 0.6$. Downstream of this point, there are larger differences between

Please cite this article in press as: Schwarze R et al. Starting jet flows in a three-dimensional channel with larynx-shaped constriction. Comput Fluids (2011), doi:10.1016/j.compfluid.2011.03.016

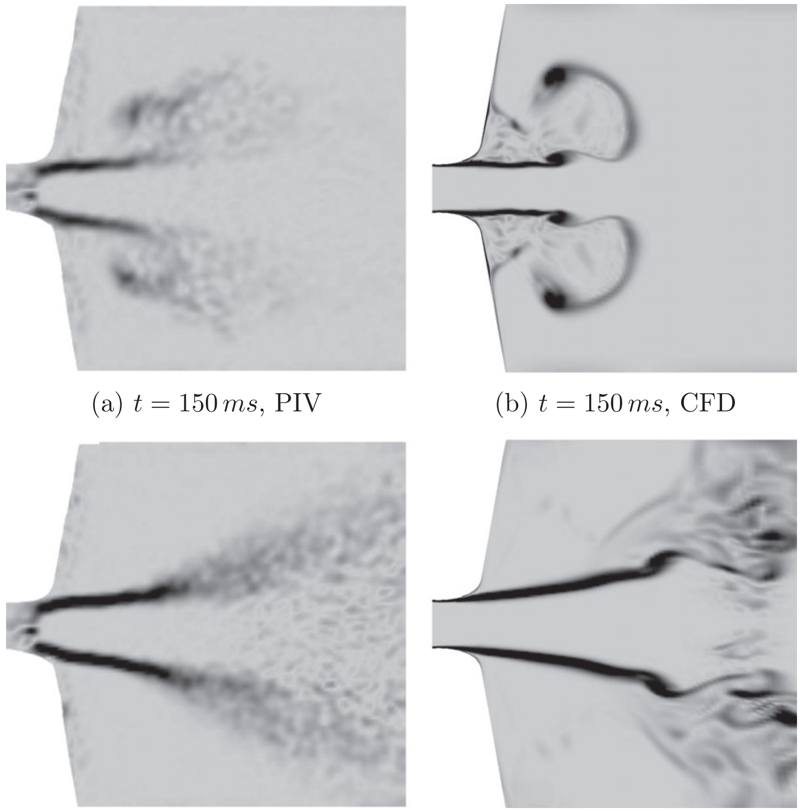

(a) $t = 150\,ms$, PIV (b) $t = 150\,ms$, CFD (c) $t = 600\,ms$, PIV (d) $t = 600\,ms$, CFD

Fig. 9. Jet development in the minor plane, indicated by $\|\Omega_z\|$ with the scale in Fig. 7c.

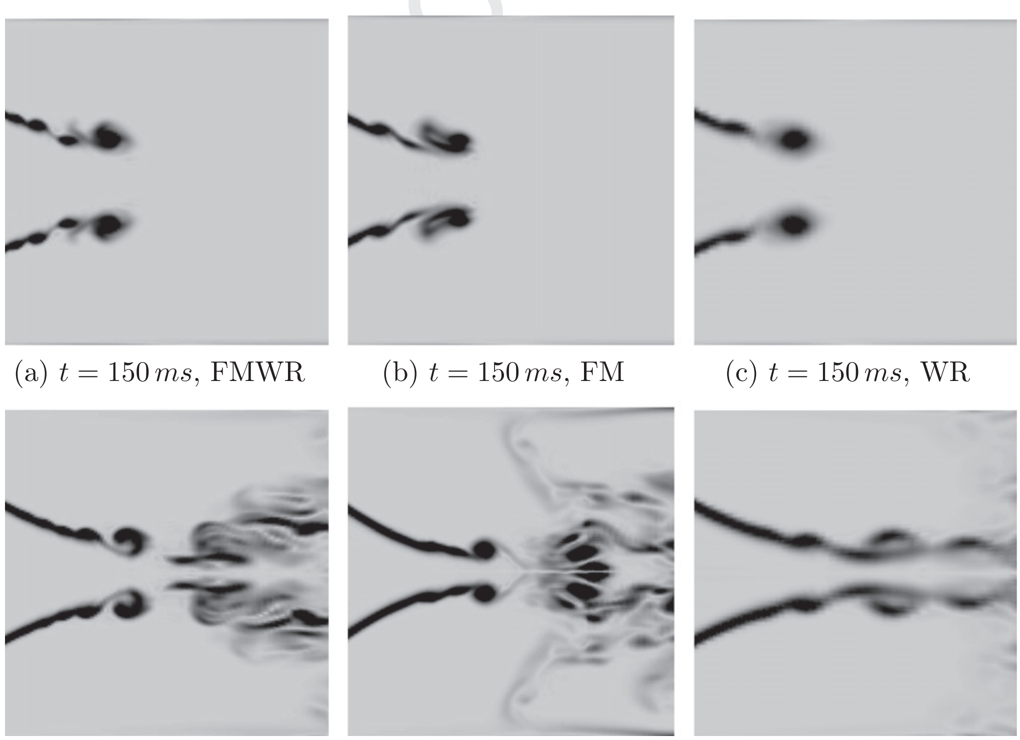

(a) $t = 150\,ms$, FMWR (b) $t = 150\,ms$, FM (c) $t = 150\,ms$, WR (d) $t = 600\,ms$, FMWR (e) $t = 600\,ms$, FM (f) $t = 600\,ms$, WR

Fig. 10. Flow resolution in major plane with the CFD model on different numerical grids, indicated by $\|\Omega_y\|$ with the scale in Fig. 7c.

Please cite this article in press as: Schwarze R et al. Starting jet flows in a three-dimensional channel with larynx-shaped constriction. Comput Fluids (2011), doi:10.1016/j.compfluid.2011.03.016

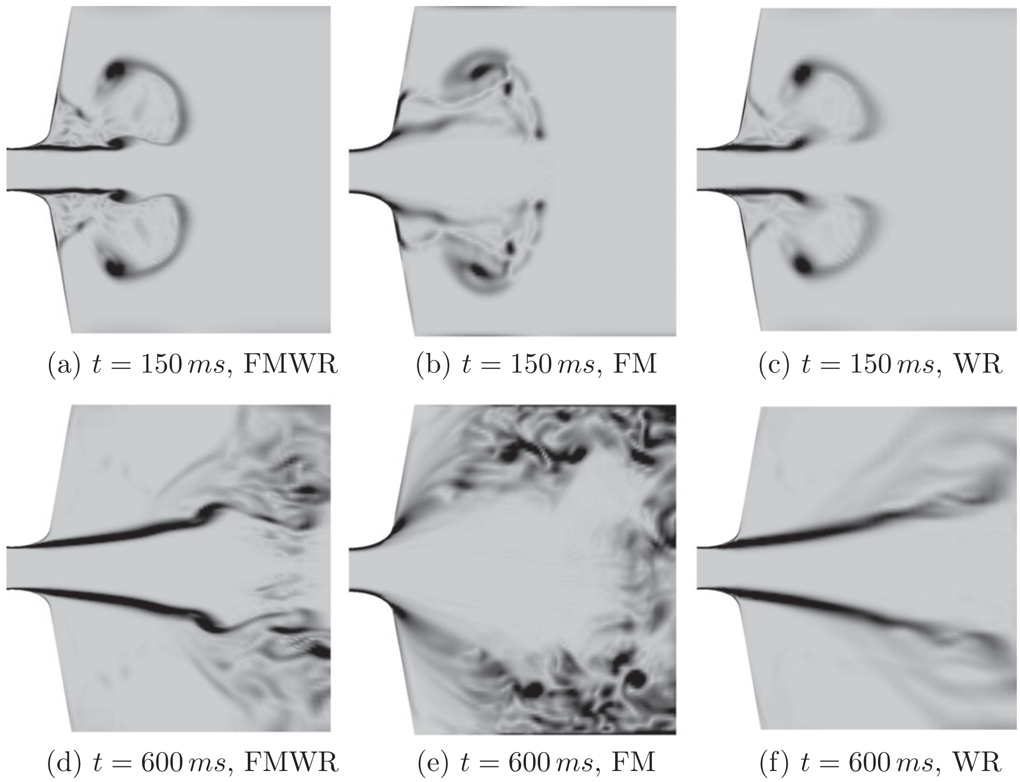

Fig. 11. Flow resolution in minor plane with the CFD model on different numerical grids, indicated by $\|\Omega_z\|$ with the scale in Fig. 7c.

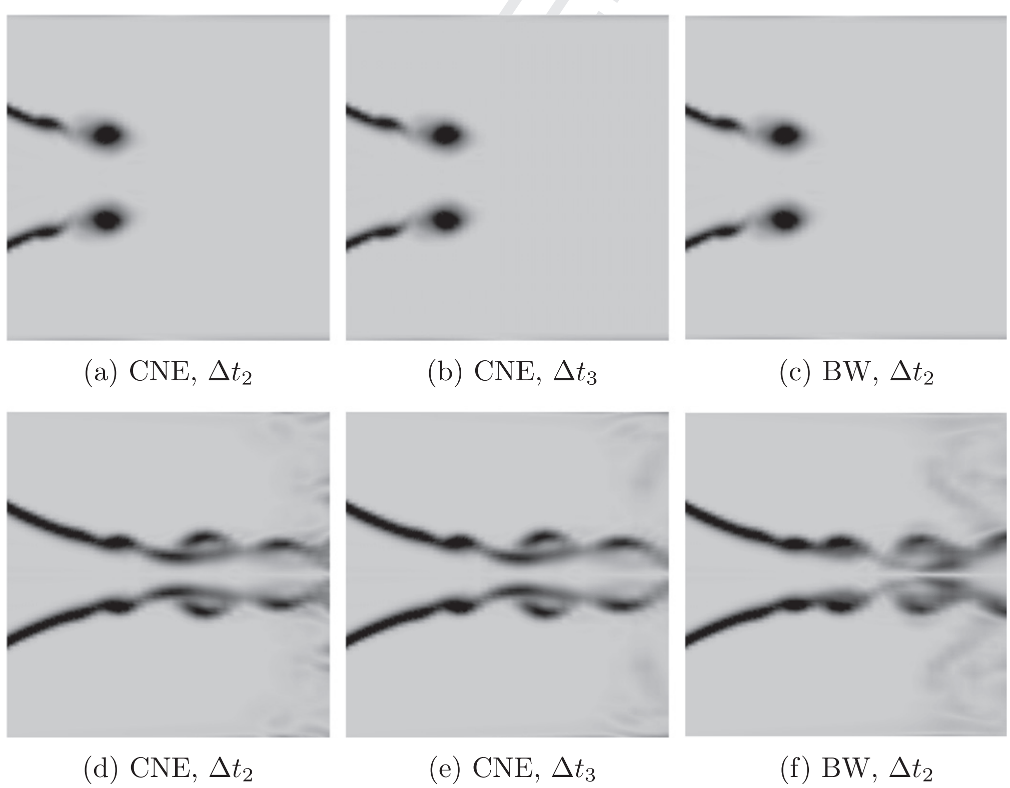

Fig. 12. Influence of time integration scheme and time-step width on the flow resolution in major plane on grid WR, indicated by $\|\Omega_y\|$ with the scale in Fig. 7c, first row: $t = 300$ ms, second row: $t = 600$ ms.

the numerical results of FMWR and WR, and both data sets differ noticeably to the PIV measurements. Obviously, the results on grid FMWR and WR are not in phase, whereas the amplitudes and lengths of the wave trains are similar on both grids.

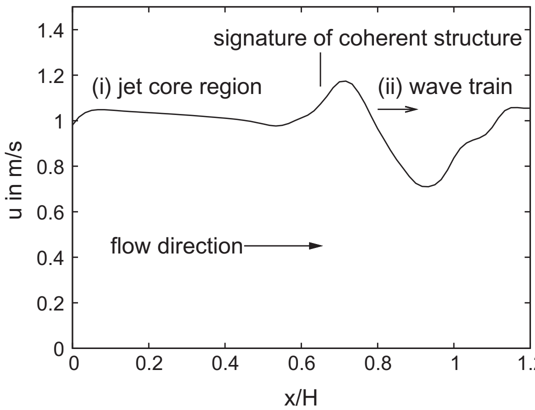

Fig. 13. Velocity profile $u(x/H)$ from CFD model on grid FMWR at $t = 450$ ms along baseline P1 (x-axis).

On the contrary, the numerical results of grid FM exhibit more pronounced differences in both the phases and the amplitudes with respect to the numerical data of the other grids and the PIV measurements. Especially the jet core velocity is underpredicted immediately downstream of the glottis, which is a consequence of the stronger deceleration of the jet flow in this region, see Fig. 9.

Fig. 15 also correlates the numerical and experimental velocity profiles at baseline P1, but here the numerical simulations are carried out with four different time-step sizes ($\Delta t_1 \ldots \Delta t_4$) and two different integration schemes (CNE, BW) on the same grid (WR). Obviously, the results of case WR, CNE in Fig. 15a show convergent behavior for decreasing time-step width. The differences between Δt_2,Δt_3 and Δt_4 are only marginal at the end of the simulation period at $t = 600$ ms. Here only the results of the simulation with the largest time-step width Δt_1 differ noticeable in phase and magnitude. The results of case WR, BW in Fig. 15b show the same tendency, but here velocity profiles in the simulations with Δt_1 and Δt_2 differ from the corresponding profiles for Δt_3 and Δt_4.

Fig. 16 shows the influence of the grid and the time integration scheme on the simulation results. Obviously, there is a good agreement of the profiles on grid WR for simulations with BW (Δt_3,Δt_4) and CNE (Δt_2,Δt_3,Δt_4), see Fig. 16a. On the other hand, the differences between the two grids FMWR and WR for simulations with a fixed time integration scheme are nearly independent from the time-step size of the simulation, see Fig. 16b. Therefore, we conclude that convergence of the results from different grids cannot be achieved, whereas the influence of the time integration scheme is of minor importance for the simulation results.

Nevertheless we assume that the characteristic change of the velocity profile for $x/H > 0.6$ is primarily due to the transitional and nonlinear behavior, whereas the numerical resolution has only a minor impact on the characteristic shape of the profile. The transition is introduced to the flow by the two touching shear layers at $x/H \simeq 0.6$ and small numerical fluctuations are strongly amplified downstream of this point. Because these numerical fluctuations are different on grids FMWR and WR, distinct specific amplitudes are observed on these grids. In the experiments, a corresponding

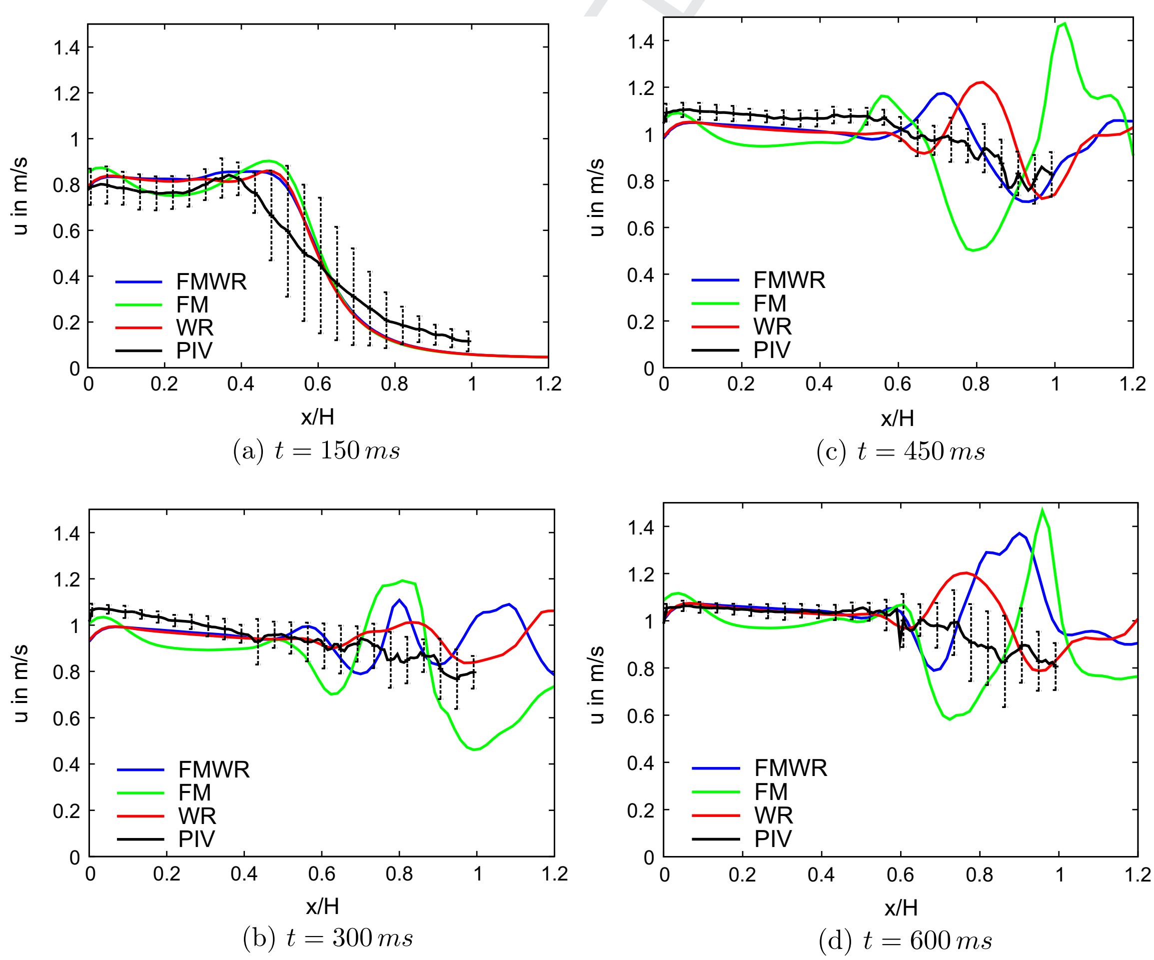

Fig. 14. Development of $u(x/H)$ along along baseline P1 (x-axis), comparison of PIV measurement and CFD model results from simulation with CNE and Δt_2.

Please cite this article in press as: Schwarze R et al. Starting jet flows in a three-dimensional channel with larynx-shaped constriction. Comput Fluids (2011), doi:10.1016/j.compfluid.2011.03.016

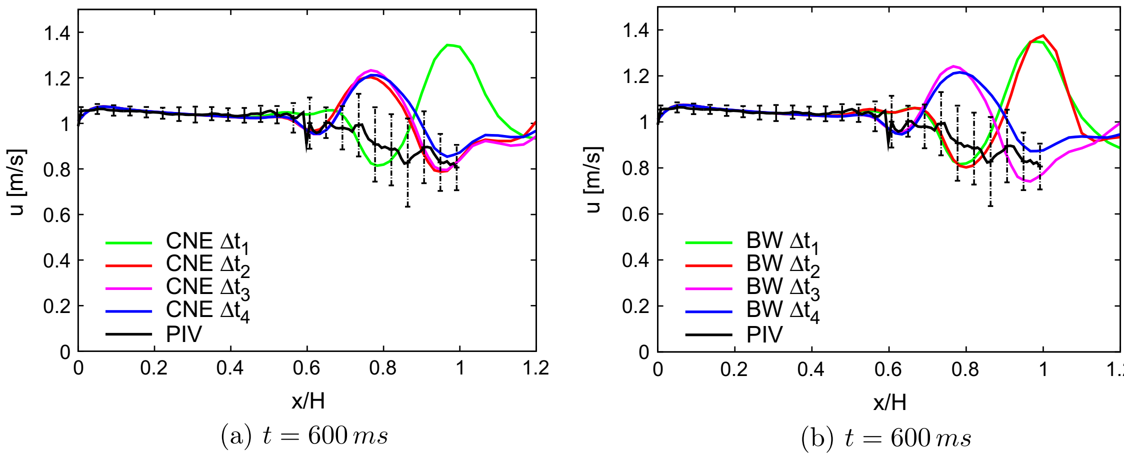

Fig. 15. Development of $u(x/H)$ along baseline P1 (x-axis), comparison of PIV measurements and simulation results on grid WR with CNE and BW and different time-step sizes, respectively.

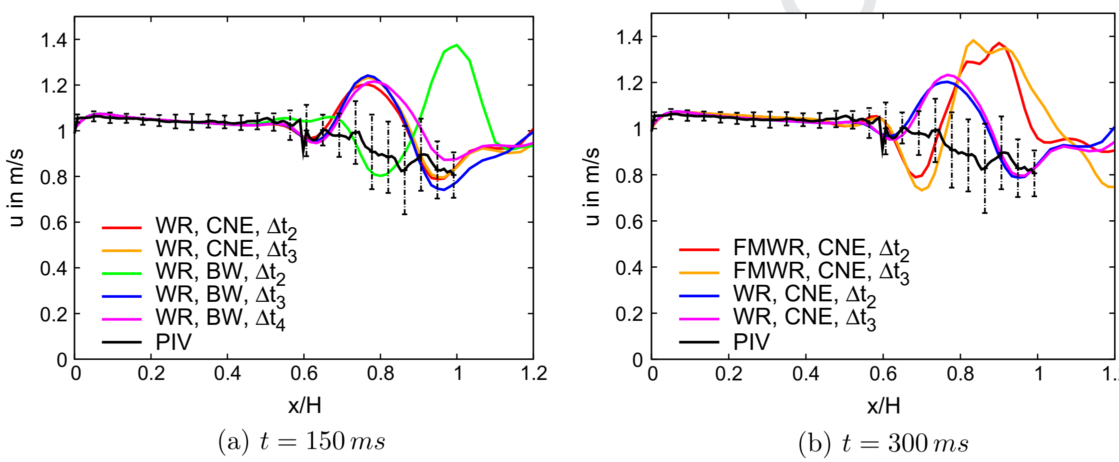

Fig. 16. Development of $u(x/H)$ along baseline P1 (x-axis), comparison of simulation results for different grids and different time discretization, respectively.

transition is indicated by the increasing rms values for $x/H \simeq 0.6$, see e. g. sub Figs. 14c and d.

Fig. 17 gives an estimation of the mean-square error, which results from amplification of the small numerical disparities. Here, the averaged results from the numerical simulations (SIM) from eight different cases (grids FMWR and WR with integration schemes CNE and BW for time-step sizes Δt_2 and Δt_3, respectively) with their mean deviations are compared with the ensemble-averaged PIV measurements. Obviously the spreading of the numerical results, which is observed only for $x/H \geqslant 0.6$, increases with time. Again, the overall agreement between SIM and PIV is acceptable. However we admit that the numerical data set is not really an ensemble in a physical sense, therefore the interpretation of Fig. 17 must be done carefully.

Fig. 18 compares the numerical and experimental velocity profiles $u(y/H)$ at baseline P2 near to the glottis for two different flow times t. Note that spurious leakage currents have been observed in the experiment near the upper and lower wall which are due to non-perfect contact of the ceiling. The figures show typical jet profiles with the high velocity jet core region around $y/H = 0$, steep jet shear layers approximately at $y/H \simeq \pm 0.1$ and the ambient fluid at rest. The numerical simulations on grids FMWR and WR fit again well to the experimental measurements in both subfigures. Here the numerical simulation on grid FM clearly underpredicts the jet core velocity, whereas the width of the jet is drastically overpredicted.

Fig. 19 compares the numerical and experimental velocity profiles $u(z/H)$ at baseline P3 for two different flow times t. Again, leakage currents are observed in the experiment. The figures show again typical features of jet profiles, the high velocity jet core region around $z/H = 0$ and steep jet shear layers approximately at $z/H \simeq \pm 0.1$. As in Fig. 18, the numerical simulations on grids FMWR and WR fit well to the experimental measurements in both subfigures. Here the numerical simulation on grid FM gives a good resolution of the jet profile for $t = 150$ ms, but at $t = 600$ ms, the jet core velocity and the width of the jet are again underpredicted.

In summary, we expect, that our numerical model with proper chosen time discretization will give a resonable description of the dynamics of large coherent structures in the developing flow. Velocity amplitudes and characteristic length scales of the structures should be sufficiently resolved in order to understand the basic features of the vortex kinematics and dynamics. However, a more detailed inspection of the fine scale interactions in the intermediate vortex field would demand a refined numerical model.

3.3. Near glottis flow

3.3.1. Glottal boundary layer

When the flow is accelerated through the glottis, laminar boundary layers develop at the vocal folds. Fig. 20 gives details of the boundary layers at $x = 0, z = 0$, where profiles of $u/u_{max}(y^+)$ are given along the minor (y) axis of the glottis. Here y^+ is determined

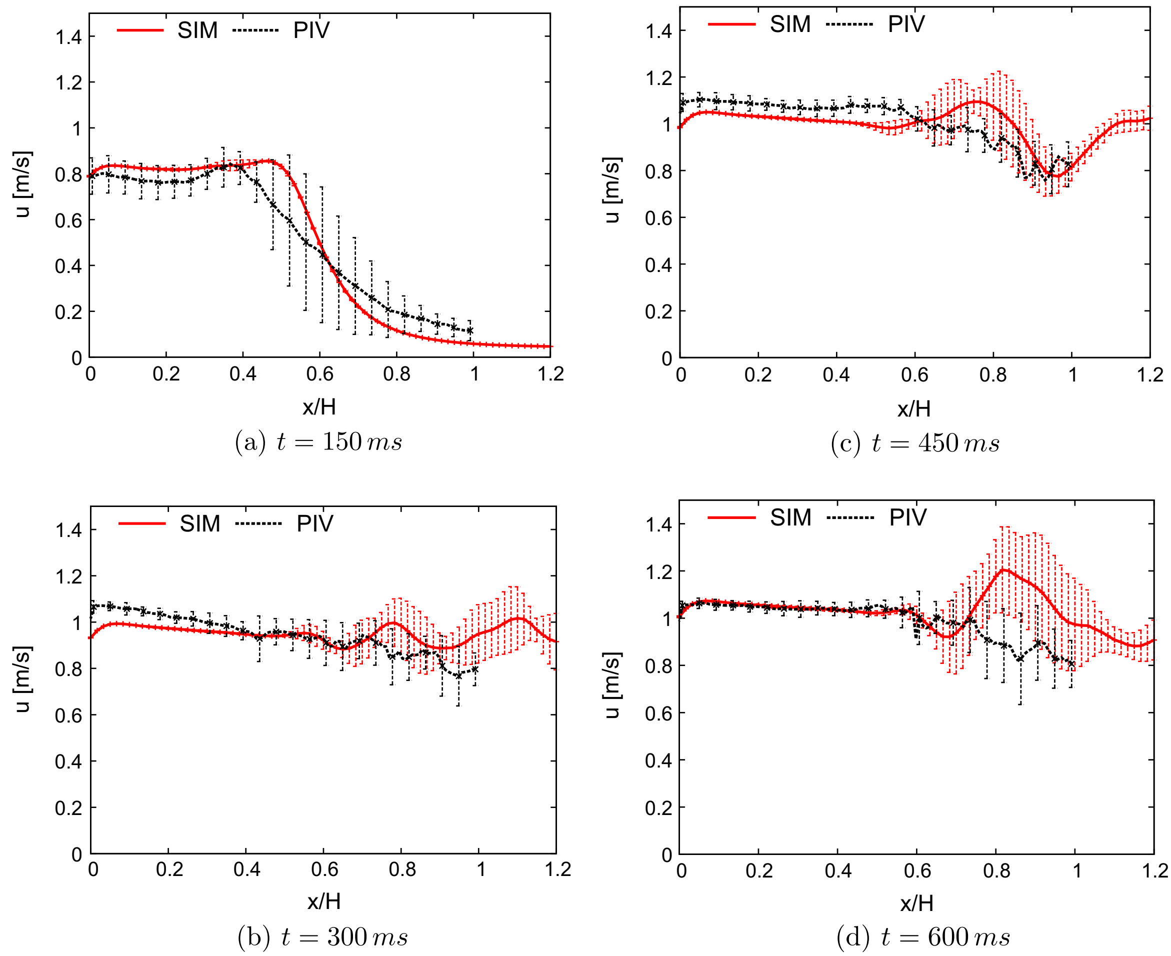

Fig. 17. Development of $u(x/H)$ along baseline P1 (x-axis), comparison of ensemble-averaged PIV measurements and averaged simulation results (SIM).

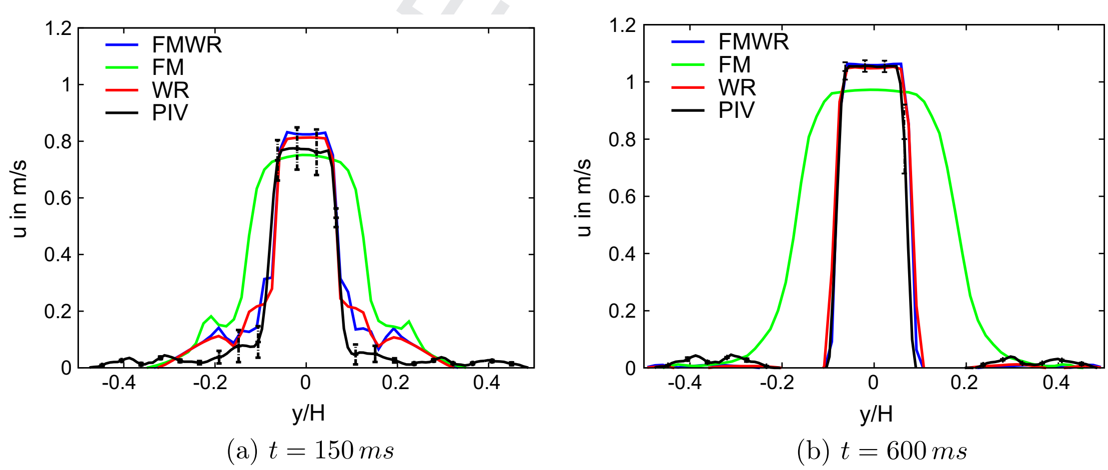

Fig. 18. Development of $u(y/H)$ along baseline P2, comparison of PIV measurement with CFD model results from simulations with CNE and Δt_2.

with the instantaneous local wall shear stresses τ_W at the glottis and u/u_{max} is referred to the instantaneous maximum velocity u_{max} which is observed in the glottis.

Obviously, shear layer profiles are resolved nearly identically on both grids FMWR and WR (starting at $y^+_{min} \simeq 2$ in the center of the wall-nearest cell). PIV measurements are not possible in this region of the experiment, therefore a comparison with experimental data cannot be given.

In Fig. 20, the linear profile $(u/u_{max})_{lin} = 0.0764\ y^+$ is also indicated as a dashed line starting at $y^+ = 0$. The comparison of the linear and the FS profile reveals a point of inflexion near $y^+ \simeq 2$, which suggests that the flow downstream of the glottis will become crit-

Please cite this article in press as: Schwarze R et al. Starting jet flows in a three-dimensional channel with larynx-shaped constriction. Comput Fluids (2011), doi:10.1016/j.compfluid.2011.03.016

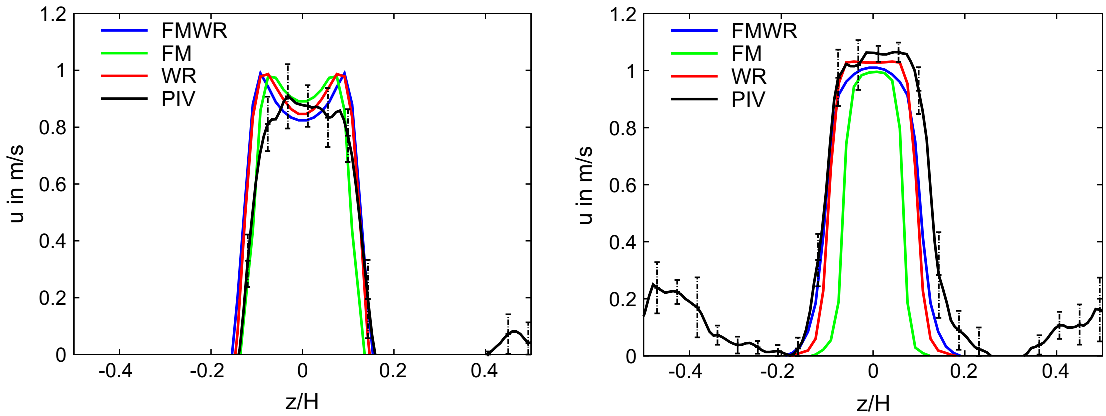

(a) $t = 150\,ms$ (b) $t = 600\,ms$

Fig. 19. Development of $u(z/H)$ along baseline P3, comparison of PIV measurement with CFD model results from simulations with CNE and Δt_2.

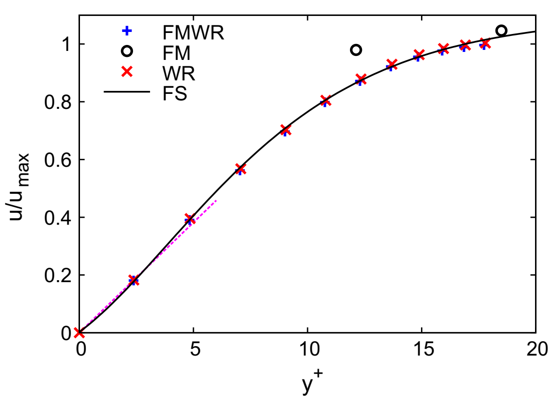

Fig. 20. Boundary layer $u/u_{max}(y^+)$ along minor axis at $x = 0$, $z = 0$ (in the smallest cross section of the glottis).

ical for separation, because $d(u/u_{max})/dy^+ \rightarrow 0$ for $y^+ = 0$. Additionally, the separated free shear layer is prone to transitional behavior due to the point of inflexion.

Although we have no possibility to give a validation by comparison with experimental data, we are convinced that the boundary layer is sufficiently resolved by the numerical grids FMWR and WR. The important scale, i.e. the boundary layer thickness is similar on both grids. The slight deviation between the profile slopes seems to be due to the different resolution of the jet core regions, which have to be matched at the outer boundary layers.

On the contrary, the resolution of the shear layer profile on grid FM is inappropriate (it starts with $y^+_{min} = 12$ in the center of the wall-nearest cell). Therefore, results from grid FM are no longer discussed in the paper.

3.3.2. Flow separation

At some distance downstream of the smallest cross section, the boundary layers separate from the vocal folds. The separation line on the lower vocal fold is investigated in Fig. 21. Due to the acceleration of the boundary layer, the location of the separation line is determined using the MRS criterion for the streamwise velocity u_s, i.e. $\partial u_s/\partial n = 0$ at $u_s = 0$ [38].

The resolution of the separation line on grids WR and FMWR is nearly identical, only small differences (below 1% with repect to D) are observed, see Fig. 21. At the touching vocal folds, the boundary layers separate immediately from the contour, whereas in the center line of the vocal fold, the separation occurs further downstream at $x/H \simeq 0.05$. The profile shows two additional bumps in the vicinity of the touching vocal folds at $z/D = \pm 0.04$, which indicate a localized shifting of the separation. This shifting originates from the inward directed displacement of the flow due to the touching vocal folds, which adds momentum to the boundary layer at these points.

The time integration scheme and the time-step width have no observable influence of the resolution of the separation line on a specific grid, see Fig. 21b. Here, the results from simulations with CNE and BW with Δt_3 and Δt_4 show only negligible differences.

3.4. Glottal Jet

3.4.1. Leading vortex

Similar to starting round jets, the starting jet flow which develops downstream of the glottis consists of a leading vortex and a trailing jet, see Fig. 7. We apply the method described in [16,17] in order to study the formation of the leading vortex in more detail. The leading vortex is detected by the inspection of the isocontours in the vorticity fields in the major, see Fig. 22. The leading vortex and the trailing shear layers are indicated by high values of vorticity, but these structures are separated by a region of lower vorticity, which is clipped in the figure.

The total circulation Γ_{tot} is calculated by integrating the vorticity in the entire major plane. The circulation of the leading vortex Γ_{lv} is estimated by integrating the vorticity inside an isocontour of vorticity that includes the leading vortex. Although this procedure is carried out to the best of our judgement, the evaluation of the vortex circulation is more subjective, especially before a clear pinch-off can be observed.

Fig. 23 shows Γ_{tot} and Γ_{lv} which is found in the major plane. Both simulations on grids FMWR and WR give nearly the same slopes of Γ_{tot} and Γ_{lv}. Γ_{tot} increases nearly uniformly due to the continuous entrainment of the separated boundary layers as free shear layers into the flow domain. Contrary Γ_{lv} is found to be constant for $9 \leqslant t^* \leqslant 15$. Then, a slight increase of Γ is observed for $t^* > 15$, but there is also an increasing uncertainty in these values. Due to the increasing complexity of the structure of the leading vortex, the determination of Γ becomes more and more difficult. Finally, we cannot specify reliable values for Γ for $t^* > 20$.

According to Gharib et al. [16], the separation of the leading vortex is determined by extrapolation from the curve of Γ_{lv}. The separation of the leading vortex from the trailing jet is expected at a dimensionless formation time or formation number $t^* = U_m \times t/d_{jet} \sim 5$ with $U_m(t) = 1/t \int_0^t u^{in}(t)dt$. A similar investigation of Γ_{tot} and Γ_{lv} in the minor planes confirms this result, which is also in agreement with the findings of Gharib et al. [16] for round jets.

Please cite this article in press as: Schwarze R et al. Starting jet flows in a three-dimensional channel with larynx-shaped constriction. Comput Fluids (2011), doi:10.1016/j.compfluid.2011.03.016

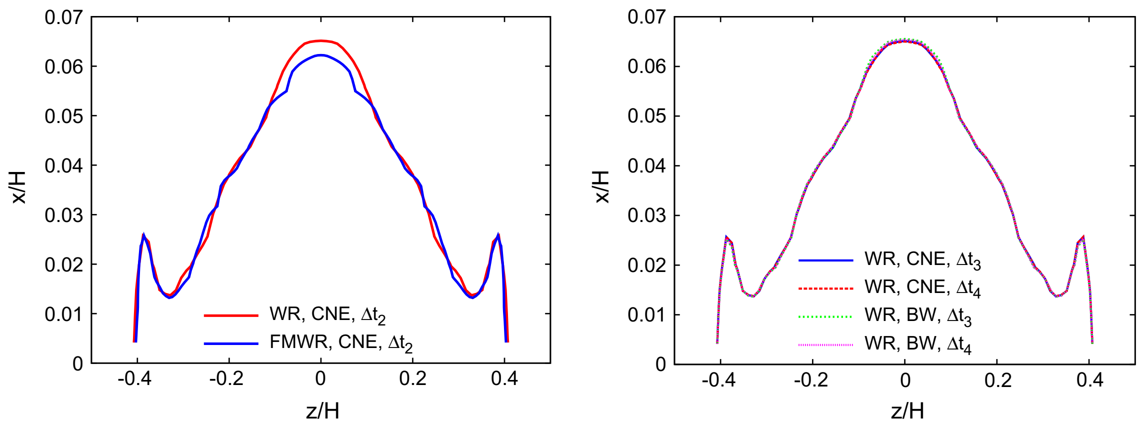

(a) Grids FMWR and WR (b) Grid WR

Fig. 21. Location of the separation lines at the lower vocal fold for t = 450 ms (top view on the vocal fold).

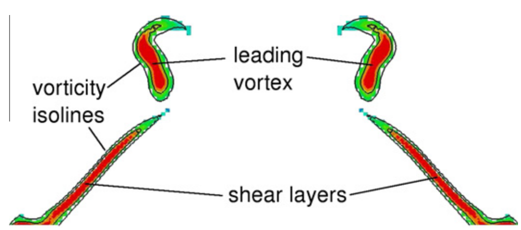

Fig. 22. Detection of the leading vortex: vorticity field in the major plane on grid FMWR, colored are regions with vorticity $\|\Omega_z\| \geqslant 200\ s^{-1}$, blue colors indicate low values, red colors indicate high values of the vorticity, flow direction is from bottom to top. (For interpretation of the references to color in this figure legend, the reader is referred to the web version of this article.)

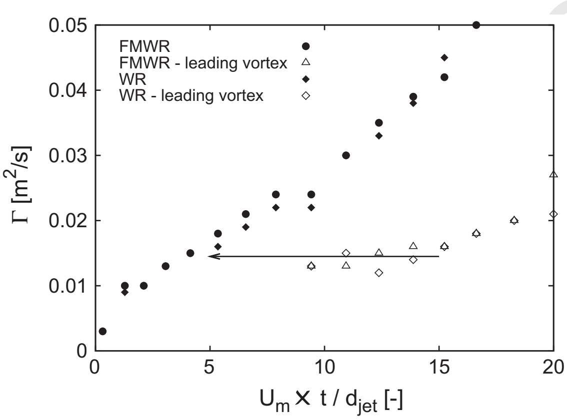

Fig. 23. Circulation Γ in the major plane as a function of dimensionless formation time $U_m \times t/d_{jet}$ on grids FMWR and FM, black symbols give the total circulation, open symbols give the circulation of the leading vortex, $U_m \times t/d_{jet} = 10$ corresponds to flow time t = 95 ms.

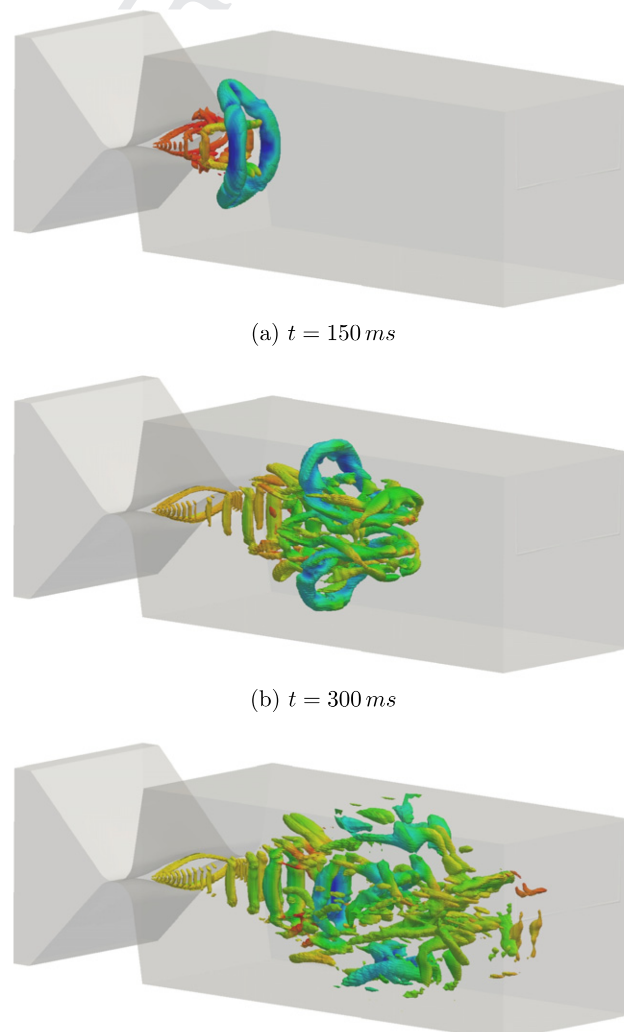

(a) $t = 150\,ms$

(b) $t = 300\,ms$

(c) $t = 450\,ms$

Fig. 24. Vortical flow structures of the starting supraglottal jet, visualized by the Q criterion with isosurfaces $Q = 10^4$. Isosurfaces are color-coded with relative pressure p (blue is $p = -200$ Pa, red is $p = 0$ Pa) with respect to ambient pressure.(For interpretation of the references to color in this figure legend, the reader is referred to the web version of this article.)

3.4.2. Vortex kinematics and dynamics

The development of the vortex field in the starting glottal jet flow is illustrated in Fig. 24. In the figures characteristic vortex structures in the transient flow are visualized by the Q criterion [37]. Here, isosurfaces with $Q = 10^4$ are colored with the local relative pressure, which is given with respect to ambient pressure. Obviously the leading vortex induces a marked pressure drop in the flow, Fig. 24a, whereas the secondary vortices which develop in the shear layers of the trailing jet do not exhibit a noticeable underpressure. During the transient development, the vortices

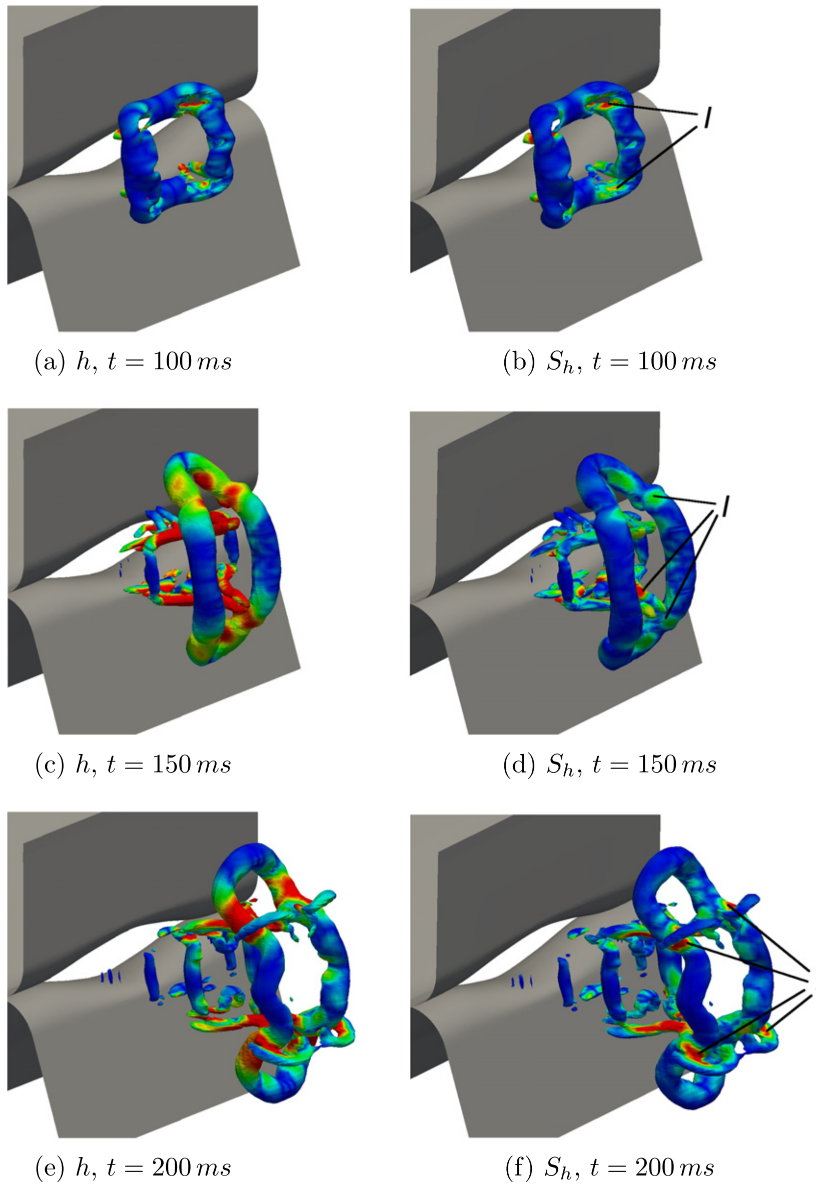

Fig. 25. Vortical flow structures of the starting supraglottal jet, visualized by the Q criterion with isosurfaces $Q = 10^4$. Isosurfaces are color-coded with magnitude of helicity density $\|h\|$ (blue is $\|h\| = 0$, red is $\|h\| = 100\ m/s^2$) or with magnitude of source $\|S_h\|$ of h (blue is $\|S_h\| = 0$, red is $\|S_h\| = 5 \cdot 10^4\ m/s^3$), respectively. (For interpretation of the references to color in this figure legend, the reader is referred to the web version of this article.)

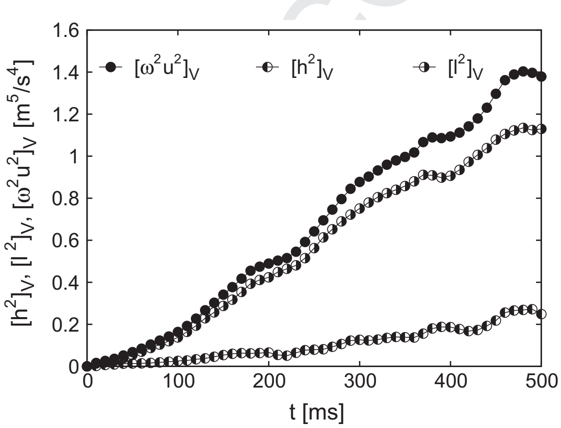

Fig. 26. Volume integrals $[\Omega^2 u^2]_V$, $[h^2]_V$ and $[l^2]_V$ as a function of t.

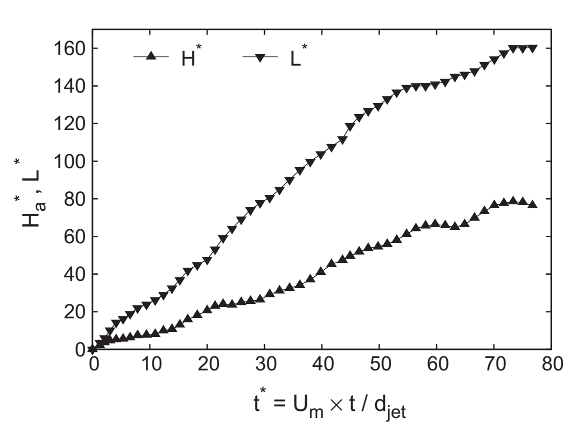

Fig. 27. Dimensionless absolute helicity H^*_a and Lamb vector integral L^* as a function of t^*.

interact strongly, Fig. 24b and c, whereby the pressure drop in the flow is somewhat smoothed.

The dynamics of the developing glottal jet and the interactions between the jet and the leading vortex can be analyzed in more detail by the investigation of the helicity density $h = \underline{\Omega} \cdot \underline{u}$. We use h as an indicator for the relationship between the directions of flow and rotation. We expect that a change of h will be a sign of the interaction between vortices. In the incompressible flow, h obeys [39,40]

$$\frac{\partial h}{\partial t} = \underbrace{\frac{\partial}{\partial x_i}\left[-h\, u_i + \left(\frac{u_j^2}{2} - \frac{p}{\rho}\right)\Omega_i + \nu\,\frac{\partial h}{\partial x_i}\right] - 2\nu\,\frac{\partial u_j}{\partial x_i}\,\frac{\partial \Omega_j}{\partial x_i}}_{S_h} \quad (3)$$

We have investigated both h and its source terms S_h, i.e. the right-hand side of Eq. (3) in the flow. As an example, Fig. 25 shows the organized vortex structures in the near-glottis region transient flow, which are again resolved by the Q criterion. Here, the isosurfaces of Q are colored with $\| h\|$ and $\|S_h\|$, respectively. Clearly, high values of $\| S_h\|$ are observed in the regions, where the leading vortex interacts with secondary vortices, which develop from the shear layers of the trailing jet. Some of these localized regions are indicated by I in Figs. 25b, d and f. Consequently, the total amount of helicity density increases due to the positive source terms, as it is observed in Figs. 25a, c and e.

The helicity density together with the Lamb vector $\underline{l} = \underline{\Omega} \times \underline{u}$ give a local orthogonal decomposition of $\underline{u}$ with respect to $\underline{\Omega}$. Both h and $\underline{l}$ are related to the product of twice the specific kinetic energy $\underline{u}^2/2$ and the enstrophy $\underline{\Omega}^2$ by

$$\underline{\Omega}^2 \underline{u}^2 = |h|^2 + |l|^2 \quad (4)$$

$$\underbrace{\int_V \underline{\Omega}^2 \underline{u}^2\, dV}_{[\Omega^2 u^2]_V} = \underbrace{\int_V |h|^2\, dV}_{[h^2]_V} + \underbrace{\int_V |l|^2\, dV}_{[l^2]_V} \quad (5)$$

Fig. 26 gives the development of $[\Omega^2 u^2]_V$, $[h^2]_V$ and $[l^2]_V$ for the accelerating phase in the entire flow volume downstream of the glottis. It is found that $\underline{\Omega}^2\underline{u}^2$ is divided with a ratio of approximately 1:4 between h and $\underline{l}$. This underlines that the dynamics of the starting glottal jet has a three-dimensional nature. The helicity density, which is zero in two-dimensional and axisymmetric flow fields seems to play an important role in the physics of the glottal jet.

Fig. 27 underlines this conclusion. Here, the absolute helicity, i.e. the volume integral of the helicity magnitude $H_a = \int_V |h|\, dV$ and $L = \int_V |\underline{l}|\, dV$ are given. Based on the findings of Moffatt [41], see also [42], H_a is a measure for the knotness of the vorticity lines in a flow region V. Therefore the increase of H_a should indicate an increase of the strengths and the winding numbers of the vortex structures in the flow. In Fig. 27, H_a^* and L^* are given in dimensionless form based on U_m and d_{jet}. Again, the important increase of H_a^* demonstrates that the three-dimensional vortex interactions induce an increase of the streamwise-oriented vorticity. The scaling which was found from the empirical fit of the data is $H_a^* \sim t^*$ and $L^* \sim (t^*)^{0.8}$, the corresponding curves are also indicated in Fig. 27.

4. Summary and outlook

A numerical model of starting supraglottal jet flows is presented. The model is based on the equation of continuity and the Navier–Stokes equations for incompressible flows. Transient simulations of the starting jet flows in the supraglottal channel are carried out. The geometry, boundary conditions and initial values of the flow fit to a corresponding model experiment which is discussed elsewhere.

The numerical model is implemented into the open source code OpenFOAM. As discretization schemes, the combination of a second-order TVD scheme and a blended Crank–Nicolson and Euler implicit scheme are employed for flux interpolation and time integration, respectively. The numerical setup is assumed to realize a blending between a direct computation of the laminar flow regions and an implicit Large-Eddy Simulation for the transitional and the turbulent flow regions.

Qualitative and quantitative comparison of numerical and experimental data show, that the numerical model is able to resolve the flow field correctly. A grid variant study shows, that the near-wall grid resolution should be fine enough in order to resolve the flow separation and the corresponding jet development adequately.

The simulations give detailed insight into the structure of the developing flow field, which is composed of the glottal region, the leading vortex and the trailing jet flow. Boundary layer profiles of the flow in the glottis, the separation line on the vocal folds, velocity profiles of the jet flow and the jet flow region are analyzed.

The boundary layers in the glottal flow region are similar to the boundary layers of the flow through a wedge nozzle. The separation line of the jet flow from the diverging vocal folds remains nearly constant throughout the transient development of the flow.

The large coherent vortex structures of the trailing jet interact strongly with the leading vortex, which is indicated by a marked rise of helicity density during the jet development. Both the Lamb vector integral and the helicity in the supraglottal flow region are found to increase nearly constantly over the complete starting period of the jet flow.

Future studies should be focused on the following topics:

- Realistic flow rate functions should be applied. The focus of the present study is to develop a suitable numerical model for three-dimensional simulations of supraglottal jet flows and to resolve basic structures and transition processes in these flows. Therefore, long-term simulations with oscillating flow rates should be an interesting continuation of our work. In this context, dynamic grids should be implemented which model the oscillating movement of the vocal folds.
- The development of the Lamb vector and the helicity should be analyzed in more detail because of the importance of the Lamb vector for the acoustics of the glottal jet.
- The flow simulations should be coupled to calculations of the acoustic field in order to analyze the process of sound generation in more detail. Here, as a first step, the acoustic source terms must be deduced from the flow data.

Acknowledgements

The authors thank the German Science Foundation DFG for funding the research under Grant No. BR 1494/13-1.

References

[1] Sciamarella D, Le Quere P. Solving for unsteady airflow in a glottal model with immersed moving boundaries. Eur J Mech B/Fluids 2008;27:42–53.
[2] Alipour F, Scherer RC. Flow separation in a computational oscillating vocal fold model. J Acoust Soc Am 2004;116:1710–9.
[3] Decker GZ, Thomson SL. Computational simulations of vocal fold vibration: Bernoulli versus Navier–Stokes. J Voice 2007;21:273–84.
[4] Tao C, Zhang Y, Hottinger DG, Jiang JJ. Asymmetric airflow and vibration induced by the Coanda effect in a symmetric model of the vocal folds. J Acoust Soc Am 2007;121:2270–8.
[5] Suh J, Frankel SH. Numerical simulation of turbulence transition and sound radiation for flow through a rigid glottal model. J Acoust Soc Am 2007;121:3728–39.
[6] Li S, Scherer RC, Wan MX, Wang SP, Wu HH. Numerical study of the effects of inferior and superior vocal fold surface angles on vocal fold pressure distributions. J Acoust Soc Am 2006;119:3003–10.

[7] Duncan C, Zhai G, Scherer RC. Modeling coupled aerodynamics and vocal fold dynamics using immersed boundary methods. J Acoust Soc Am 2006;120:2859–71.
[8] Bae Y, Moon YC. Computation of phonation aeroacoustics by an INS/PCE splitting method. Comput Fluids 2008;37:1332–43.
[9] Zheng X, Bielamowicz S, Luo HX, Mittal R. A computational study of the effect of false vocal folds on glottal flow and vocal fold vibration during phonation. Ann Biomed Eng 2009;37:625–43.
[10] Larsson M, Müller B. Numerical simulation of confined pulsating jets in human phonation. Comput Fluids 2009;38:1375–83.
[11] Triep M, Brücker Ch, Schröder W. High-speed PIV measurements of the flow downstream of a dynamic mechanical model of the human vocal folds. Exp Fluids 2005;39:232–45.
[12] Neubauer J, Zhang Z, Miraghaie R, Berry DA. Coherent structures of the near field flow in a self-oscillating physical model of the vocal folds. J Acoust Soc Am 2007;121:1102–18.
[13] Drechsel JS, Thomson SL. Influence of supraglottal structures on the glottal jet exiting a two-layer synthetic, self-oscillating vocal fold model. J Acoust Soc Am 2008;123:4434–45.
[14] Renotte C, Bouffioux V, Wilquem F. Numerical 3D analysis of oscillatory flow in the time-varying laryngeal channel. J Biomech 2000;33:1637–44.
[15] Brouns M, Verbanck S, Lacor C. Influence of glottic aperture on the tracheal flow. J Biomech 2007;40:165–72.
[16] Gharib M, Rambod E, Shariff K. A universal time scale for vortex ring formation. J Fluid Mech 1998;360:121–40.
[17] Rosenfeld M, Rambod E, Gharib M. Circulation and formation number of laminar vortex rings. J Fluid Mech 1998;376:297–318.
[18] Shusser M, Gharib M. Energy and velocity of a forming vortex ring. Phys Fluids 2000;12:618–21.
[19] Mohseni K, Ran H, Colonius T. Numerical experiments on vortex ring formation. J Fluid Mech 2001;430:267–82.
[20] Krueger PS, Gharib M. The significance of vortex ring formation to the impulse and thrust of a starting jet. Phys Fluids 2003;15:1271–81.
[21] Gao L, Yu SCM. A model for the pinch-off process of the leading vortex ring in a starting jet. J Fluid Mech 2010;656:205–22.
[22] Margolin LG, Rider WJ, Grinstein FF. Modeling turbulent flows with implicit LES. J Turbul 2006;7:1–27.
[23] Grinstein FF, Margolin LG, Rider WJ. Implicit large eddy simulation. New York: Cambridge University Press; 2007.
[24] Grinstein FF, DeVore CR. Dynamics of coherent structures and transition to turbulence in free square jets. Phys Fluids 1996;8:1237–51.
[25] Drikakis D, Fureby C, Grinstein FF, Hahn M, Youngs D. LES of transition to turbulence in the Taylor Green vortex. In: Proccedings of 6th International ERCOFTAC Workshop on Direct and Large-Eddy Simulation. Dordrecht (NL): Springer; 2006. p. 159–66.
[26] OpenCFD Ltd. OpenFOAM 1.5 documentation. <http://www.opencfd.co.uk/openfoam/doc/index.html>.
[27] van Leer B. Towards the ultimate conservative difference scheme. V. A second-order sequel to Godunov's method. J Comput Phys 1979;32:101–36.
[28] Fureby C. ILES and LES of complex engineering turbulent flows. J Fluids Eng 2007;129:1514–23.
[29] Grinstein FF, Fureby C, DeVore CR. On MILES based on flux-limiting algorithms. Int J Numer Methods Fluids 2005;47:1043–51.
[30] Issa RI. Solution of the implicit discretized fluid flow equations by operator splitting. J Comp Phys 1985;62:40–65.
[31] Rhie CM, Chow LW. Numerical study of the turbulent flow past an airfoil with trailing edge separation. AIAA J 1983;21:1525–32.
[32] Fletcher RW. Conjugate gradient methods for indefinite systems. Lect Notes Math 1976;506:73–89.
[33] Karypis G, Kumar V. A fast and high quality multilevel scheme for partitioning irregular graphs. SIAM J Sci Comp 1999;20:359–92.
[34] Karypis G, Kumar V. METIS 4.0 documentation. <http://glaros.dtc.umn.edu/gkhome/metis/metis/download>.
[35] Hussain F, Husain HH. Elliptic jets. Part 1. Characteristics of unexcited and excited jets. J Fluid Mech 1989;208:257–320.
[36] Husain HH, Hussain F. Elliptic jets. Part 2. Dynamics of coherent structures: pairing. J Fluid Mech 1991;233:439–82.
[37] Jeong J, Hussain F. On the identification of a vortex. J Fluid Mech 1995;285:69–94.
[38] Schlichting H, Gersten K. Boundary layer theory. Berlin: Springer; 2003.
[39] Yoshizawa A. Hydrodynamic and magnetohydrodynamic turbulent flows. Dordrecht: Kluwer; 1998.
[40] Holm DD, Kerr RM. Helicity in the formation of turbulence. Phys Fluids 2007;19:025101.
[41] Moffatt HJ. The degree of knottedness of tangled vortex lines. J Fluid Mech 1969;35:117–29.
[42] Wu JZ, Ma HY, Zhou MD. Vorticity and vortex dynamics. Berlin: Springer; 2006.

Please cite this article in press as: Schwarze R et al. Starting jet flows in a three-dimensional channel with larynx-shaped constriction. Comput Fluids (2011), doi:10.1016/j.compfluid.2011.03.016